

Fundamental parameters and infrared excesses of *Hipparcos* stars

I. McDonald,^{1*} A. A. Zijlstra¹ and M. L. Boyer²

¹Jodrell Bank Centre for Astrophysics, Alan Turing Building, Manchester M13 9PL

²STScI, 3700 San Martin Drive, Baltimore, MD 21218, USA

Accepted 2012 August 5. Received 2012 August 1; in original form 2012 July 9

ABSTRACT

We derive the fundamental parameters (temperature and luminosity) of 107 619 *Hipparcos* stars and place these stars on a true Hertzsprung–Russell diagram. This is achieved by comparing BT-SETTL model atmospheres to spectral energy distributions (SEDs) created from *Hipparcos*, *Tycho*, Sloan Digital Sky Survey, DENIS, Two Micron All Sky Survey, *MSX*, *AKARI*, *IRAS* and *Wide-field Infrared Survey Explorer* data. We also identify and quantify from these SEDs any infrared excesses attributable to circumstellar matter. We compare our results to known types of objects, focusing on the giant branch stars. Giant star dust production (as traced by infrared excess) is found to start in earnest around $680 L_{\odot}$.

Key words: circumstellar matter – stars: fundamental parameters – Hertzsprung–Russell and colour–magnitude diagrams – stars: mass-loss – solar neighbourhood – infrared: stars.

1 INTRODUCTION

Spectral energy distributions (SEDs) have long been the primary method of understanding stars. Colour–magnitude diagrams, which can be quickly made from photometric data, enable one to explore various facets of stellar populations, such as stellar mass and evolutionary state. However, these do not present the information at its most basic physical level: the stellar temperature and luminosity. These represent the fundamental ideals of stellar modelling and are theoretically free from biases introduced by photometric calibration, interstellar reddening and similar phenomena.

While transformations to these parameters can be achieved through colour–temperature relations and bolometric corrections, these are limited in scope. Most importantly, the wavelength coverage of the observations means that well-defined solutions do not always exist for these relations (e.g. for very red stars or for observations only covering wavelengths longer than the SED peak). Using the entire wavelength coverage available allows better determination of stellar temperature when a wide temperature range is present among a stellar sample. This also allows finer control of data quality. All-sky surveys are, in particular, prone to contain some poor-quality data due to the large flux range they are required to cover, which leads to the saturation of bright sources, and the volume of data, which limits the ability to match photometric routines to particular situations (e.g. in areas of high stellar density or nebular emission). Stellar variability can also cause improper colours to be reported, which can be reduced by using multiple epochs or, equivalently, multiwavelength data. In this manner, we can provide more robust estimates of parameters for individual objects, allowing

them to be placed on the true, physical Hertzsprung–Russell (HR) diagram.

Perhaps the greatest benefit, however, is the ability to detect excess flux at a particular wavelength, by providing a reference model flux against which fluxes in individual photometric filters can be compared. This is particularly helpful in the infrared (IR), where colour–magnitude diagrams based on only part of the SED can fail to identify sources exhibiting emission in addition to the stellar photosphere. Predominantly, these sources are either very young stars (pre-main-sequence T Tauri stars or Herbig Ae/Be stars), rapid rotators (classical Be stars) or evolved stars. This latter group is mostly comprised of mass-losing red and asymptotic giant branch (RGB/AGB) stars, on which we focus our discussion.

Previously, only colour–magnitude diagrams have been used to interpret our closest stellar neighbours (e.g. Perryman et al. 1995). We are now able to take the data returned by the *Hipparcos* satellite (Perryman & ESA 1997; van Leeuwen 2007) and match them with other all-sky surveys to produce a true HR diagram of the local Solar neighbourhood.

In doing so, we can identify and characterize stars with weak IR excesses which may be otherwise missed by conventional colour cuts. While this has been attempted previously (Ita et al. 2010; Groenewegen 2012; we later discuss these papers in context), this work represents the first time that such a process has been applied to the entire *Hipparcos* data set and in the context of the stars' absolute, fundamental parameters.

2 FUNDAMENTAL STELLAR PARAMETERS

2.1 Input data catalogue

The new *Hipparcos* (H_p)/*Tycho* (B_T , V_T) reduction (van Leeuwen 2007) was used as the primary astrometric and photometric

*E-mail: mcdonald@jb.man.ac.uk

Table 1. Number of sources used from each catalogue.

Catalogue	Wavelength (μm)	Beam size (arcsec)	Original data	Sources used combined catalogue	Final catalogue
<i>Hipparcos</i>	0.528	~ 0.5	117 956	109 661	107 616
<i>Tycho</i>	0.420, 0.532	~ 0.5	118 924	109 624	107 586
SDSS	0.354–0.623	$\gtrsim 0.5$	32 253	30 368	27 420
DENIS	0.786–2.20	$\gtrsim 0.5$	60 083	2856	2762
2MASS	1.25–2.20	$\gtrsim 0.5$	104 324	104 297	104 111
<i>MSX</i>	4.29–21.3	≈ 18.3	7663	7336	3153
<i>AKARI</i>	10.5, 18.4	2.4, 2.3	48 078	48 013	47 762
<i>IRAS</i>	12, 25	106, 106	19 728	16 001	15 533
<i>WISE</i>	3.35–22.1	5.8–11.8	64 192	64 102	63 883

Notes: the ground-based optical beam sizes of SDSS, DENIS and 2MASS are limited by seeing, and hence presented as approximate lower limits. Beam sizes of scanning satellites are not circular: here, the equivalent-sized circular aperture is given instead. The combined catalogue contains all *Hipparcos* objects for which we were able to obtain any matching IR data. The final catalogue contains only the objects remaining after the data quality cuts described in Appendix A had been carried out.

catalogue, to which the other catalogues were matched. Additional data were sourced from the following surveys.

(i) Sloan Digital Sky Survey (SDSS-III) data release 8 (Aihara et al. 2011): *ugr*-band optical data were included. These data are heavily affected by saturation for the *Hipparcos* sample. The *iz*-band photometry were left out entirely, and bad data from the *ugr*-bands were identified as described in Section 2.3.

(ii) Deep Near-Infrared Survey of the Southern Sky (DENIS) Consortium 2005 data release:¹ $i_{\text{Gunn}}JK_s$ -band data were included for sources where $i_{\text{Gunn}} > 9.5$ mag. JK_s -band near-IR data were used only when Two Micron All Sky Survey (2MASS) data were not available (see below).

(iii) 2MASS all-sky catalogue of point sources (Skrutskie et al. 2006): JHK_s -band near-IR data were included. All photometry was initially included, regardless of data quality: bad data were later removed as described in Section 2.3.

(iv) *MSX* Infrared Astrometric Catalogue (Egan & Price 1996), incorporating six bands (B_1 , B_2 , A , C , D and E) covering 4–18 μm . Note that, at ≈ 18 arcsec resolution, these data exhibit problems from source blending.

(v) The *AKARI*–*Hipparcos* cross-correlated catalogue (Ita et al. 2010), covering 9 and 18 μm , hereafter *AKARI* [9] and [18].

(vi) *IRAS* catalogue of point sources, Version 2.0 (PSC; Beichmann, Helou & Walker 1988), and faint source catalogue, $|b| > 10$, Version 2.0 (FSC; Moshir et al. 1992), both limited to the 12- and 25- μm bands, hereafter *IRAS* [12] and [25]. At ≈ 1 arcmin resolution, these data also exhibit problems from source blending.

(vii) The *Wide-field Infrared Survey Explorer* (*WISE*) preliminary data release (Wright et al. 2010), incorporating four bands (W_1 through W_4) covering 3.5–22 μm .

As the surveys cover a large range of wavelengths and have very differently sized point spread functions (PSFs; Table 1), one must be conservative in declaring two detections as arising from the same source. DENIS, 2MASS and *AKARI* detections were considered to be matched with *Hipparcos* detections when their coordinates matched to within 1 arcsec; SDSS and *WISE* data were matched when within 3 arcsec and *MSX* and *IRAS* data were matched within 5 arcsec.

Due to the differing depths and similar wavelength coverages of the near- and mid-IR catalogues, substitutions were made to choose only the most discerning data. Specifically, where possible, *MSX* and *IRAS* data were replaced by higher resolution, greater sensitivity *WISE* and *AKARI* data; also DENIS photometry was replaced by 2MASS photometry, which is less prone to saturation. These substitutions were performed as follows:

- (i) W_1 and W_2 replace *MSX* B_1 and B_2 , respectively;
- (ii) *AKARI* [9] replaces *MSX* A ;
- (iii) W_3 and/or *IRAS* [12] replaces *MSX* C and D , respectively;
- (iv) W_4 and/or *AKARI* [18] replaces *MSX* E ;
- (v) 2MASS J and K_s replace DENIS J and K_s , respectively;
- (vi) *IRAS* FSC data replace *IRAS* PSC data.

SDSS bands were dropped under certain conditions, namely

- (i) u was dropped if $u > B_T + (B_T - V_T) + 2$ mag;
- (ii) g was dropped if $g > B_T + 2$ mag;
- (iii) r was dropped if $r > V_T + 2$ mag,

which correspond to ranges beyond which the SDSS data (which are prone to saturation for the *Hipparcos* stars, most of which are comparatively bright) cannot be matched in simultaneity with the *Tycho* data to any stellar model.

The resulting initial input catalogue contains 109 661 *Hipparcos* stars with data from the u band to 25 μm . The source statistics for this combined catalogue are listed in Table 1.

2.2 Fitting the SEDs

The SEDs were fitted using the code initially described in McDonald et al. (2009) and modified in the subsequent papers (Boyer et al. 2009a; McDonald et al. 2010a,b, 2011b,d; McDonald, Johnson & Zijlstra 2011c; Woods et al. 2011). This code, hereafter referred to as GETSED, is optimized to detect low-contrast IR excess arising from circumstellar dust. We have made some further revisions to the code as detailed below.

GETSED works by minimizing the χ^2 statistic between the observed photometric data and a set of synthetic stellar spectra to determine stellar temperature and luminosity. This requires user-defined stellar mass, metallicity and distance, and an interstellar reddening, and given appropriate filter transmission curves. A grid of temperatures between 2400 and 60 000 K is set up, in steps of 400 K. Blackbodies

¹ VizieR online data catalogue: II/263.

of these temperatures are fitted to the de-reddened photometric data and the model with the lowest χ^2 chosen. A finer grid is set up and the blackbody temperature is iterated to the nearest 25 K. This temperature is then used to derive the stellar luminosity and surface gravity to first order.

For this work, we do not know the mass or metallicity of our stars, which are required to select the correct set of synthetic spectra. Nor do we know the interstellar reddening towards the stars. We assume that the metallicity is solar and that the interstellar reddening is zero. An assumption of solar metallicity is reasonable for nearby Galactic stars: the true values scatter around the solar value of $[Z/H]$ (Luck & Heiter 2005), with the scatter imparting a $\lesssim 3$ per cent error to the temperature fit for the majority of stars. The magnitude of this error is similar to that imparted by good-quality photometry.

A larger error is imparted by interstellar reddening, which makes the star appear dimmer and cooler than it actually is. This can be significant in the case of distant objects, or those in the Galactic plane. In practice, stars which suffer from significant interstellar extinction tend to be the brighter giant stars, which also suffer from significant parallax errors. Bright giants are often subject to radial pulsations. These can change the fractional contribution of cool and hotspots on the stellar surface to the star's total light, leading to changes in the astrometric centre of light. These can impart substantial parallax errors (van Leeuwen 2007), which can be sufficiently large that extinction is not the primary source of error in the placement of these stars on the HR diagram.

As we do not know the mass of individual stars, we estimate it from the best-fitting blackbody temperature and luminosity. As this only affects the stellar gravity, which has a minimal effect on the overall SED, we need to only approximate the actual mass. We estimate the stellar mass by assuming that each star is either a main-sequence star or a giant. Giants are determined to be stars with

$$L > \begin{cases} (2.25 \times 10^{-4} T)^7 & \text{if } T > 6000 \text{ K} \\ (6.5 \times 10^{-4} T)^7 & \text{otherwise,} \end{cases} \quad (1)$$

where T is the determined effective temperature in kelvin and L is the determined luminosity in solar units.

For main-sequence stars, we use a mass–temperature relation based on a solar-metallicity, zero-age main-sequence isochrone (Dotter et al. 2008). We cannot estimate the mass of giant stars so easily. Most stars below the RGB tip ($L \approx 2500 L_\odot$) will be the more-numerous, older stars of $\sim 1 M_\odot$. More massive giants survive to much higher luminosities on the AGB; thus, we expect very luminous giants to be considerably more massive. Based on the aforementioned isochrones (Dotter et al. 2008), we assume a mass for the giant stars of $M = (L/2500 L_\odot)^{2/3} M_\odot$, with limits placed at 1 and 20 M_\odot .

The first-order determinations of temperature, luminosity and stellar gravity (from the blackbody fit), are used as the initial parameters for our synthetic spectra. Previously, we have used the MARCS model atmospheres (Gustafsson et al. 1975, 2008) described in McDonald et al. (2009). For this work, however, we instead use the BT-SETTL models of Allard et al. (2003), as the temperature spacing of the grid models is finer in the 4000–6000 K region. We have found this to reduce artefacts caused by interpolation between grid points for stars with poor-quality photometry.

GETSED takes the model spectra grid and performs a linear interpolation in temperature and surface gravity (and metallicity, if required). The synthetic spectrum is convolved with the observed filter transmissions and reduced to a set of expected photometric fluxes. These are then normalized to the observed photometric

fluxes (the constant of normalization determining the luminosity) and a χ^2 is determined.

This process is first performed on the temperature grid point immediately cooler than the blackbody temperature. GETSED then calculates χ^2 for the neighbouring temperature grid points and continues until a χ^2 minimum is detected. The temperature corresponding to the χ^2 minimum is used as a new starting point, a new surface gravity is calculated and χ^2 is determined for 128 K steps between the neighbouring models. A new χ^2 minimum is determined, the temperature step is halved and the process re-run until the temperature is fit to within 1 K. The calculated stellar effective temperature, luminosity, surface gravity and model photometric fluxes are written to disc.

As with our previous uses of this code, we have only fitted photometric data with short wavelengths (here we require $\lambda < 8 \mu\text{m}$). Circumstellar dust will still cause some opacity in the optical, but the obscuration must be relatively small for it to have been observed with *Hipparcos*, and the absorption of optical flux is relatively easy to identify when it is re-radiated in the IR.

Stars which are heavily extincted will have SEDs that become double-peaked. In these cases, GETSED will not be able to fit a model spectrum to it. The most extincted stars (e.g. IRC+10216; Kwan & Hill 1977) may be sufficiently optically obscured that they do not feature in the *Hipparcos* catalogue (cf. Boyer et al. 2009b). This becomes important in the removal of bad data (see Section 2.3), and we remind the reader that our HR diagram is therefore incomplete, even at high luminosity.

2.3 Removing bad data

Each star now has a series of photometric data points for which an observed and a modelled flux are known. The ratio (R) of observed/modelled flux therefore gives the excess or deficit flux in that band. We give this as a pure ratio, rather than in terms of a σ -based excess, as we do not include the errors in the photometric data in our model. While this may appear surprising, the reported errors on photometric data are almost invariably much lower than the absolute error between catalogues. Such ‘bad’ data can be incorporated into the SED for several intrinsic and extrinsic reasons, including (in approximate order of overall severity)

- (i) poor-quality raw data, e.g. saturated images or unflagged cosmic rays;
- (ii) blending, particularly among catalogues which have integrated fluxes over different areas (e.g. the PSF of *Hipparcos* is of a very different size to that of *IRAS*), affecting binary and multiple stars, and objects which are in the same line of sight as background objects with very red colours (e.g. redshifted galaxies in IR surveys);
- (iii) poor background subtraction, which mainly affects IR observations of sources at low Galactic latitudes or in other regions of nebulousity;
- (iv) intrinsic variability among stars;
- (v) inaccurate source matching due to large proper motions;
- (vi) the accuracy of photometric corrections to each survey's base photometric system.

The issues become particularly problematic when comparing optical and mid-IR catalogues: in the mid-IR, stars typically present fainter detections compared to higher backgrounds, and beam sizes are typically larger (hence include more objects). Additional errors come from the model parameters which arise from our assumption that stars have solar metallicity, a given stellar mass and no interstellar extinction. Bearing this in mind, we have assumed that each

photometric point has an arbitrary absolute error of 10 per cent and computed a χ^2 -based goodness-of-fit measure based on this uncertainty. We also do not give error estimates for our temperatures and luminosities, as they would essentially be meaningless.

The bad data in our combined multiwavelength catalogue are mostly of sources which have saturated in the various input survey catalogues. The *WISE* catalogue, in particular, suffers from saturation. Some photometry flagged as good does not match detections in other bands (e.g. HIP 24436 has $W_2 = 1.987 \pm 0.009$ mag, while $W_{1,3,4} = 0.739, 0.001$ and -0.030 mag). Conversely, some photometry flagged as uncertain does not decrease the goodness of fit of the model SEDs and is therefore sufficiently accurate for the purpose of identifying IR excess. We have so far included all *WISE* data, regardless of their uncertainty, and we must now remove the points we believe to be in error.

Unfortunately, this is a particularly recalcitrant data set to remove bad data from: we wish to keep points which fit badly due to intrinsic variability (as these will, on average, cancel out across the SED), but remove data points which have incorrect fluxes. We have opted to apply a number of sequential cuts to remove bad quality data. Since altering one band affects the model fit of the others, we must carefully design these cuts to minimize errant removal of good quality data. At each step, we have visually examined the SEDs of the objects with the worst-fitting models and devised a cut which removes the dominant contribution of bad data. The removed data were examined and the cut was applied if it did not remove any plausibly accurate data. The details of these cuts are given in Appendix A.

While these cuts have not removed every single bad data point, they have removed the vast majority of bad data, providing a much cleaner data set with which we can work. This has sadly meant removing stars where there were not sufficient data to provide a robust fit, meaning the original *Hipparcos* catalogue has been reduced from 117 956 to 107 619 objects.

2.4 Defining IR excess

Now that we have removed bad data from our catalogue, we can calculate the amount of IR excess present for each star. Having already performed SED fitting, creating a measure of IR excess becomes a trivial exercise in comparing the fitted model with observations. Providing the best metric(s) to quantify IR excess is more difficult. We adopt two techniques.

Our first metric simply takes the ratio of the observed to SED-modelled flux of all the data longward of $2.2 \mu\text{m}$ (*WISE*, *MSX*, *AKARI* and *IRAS*) and averages them together. This provides a single number (E_{IR}) that describes the average excess in the $3\text{--}25 \mu\text{m}$ region, relative to the underlying photospheric model, which can be described mathematically as

$$E_{\text{IR}} = \sum_{\lambda > 2.2 \mu\text{m}} \frac{F_{\nu}^{\text{obs}} / F_{\nu}^{\text{model}}}{n_{\text{obs}}}, \quad (2)$$

where F_{ν}^{obs} and F_{ν}^{model} are, respectively, the observed and modelled fluxes at frequency ν (corresponding to wavelength λ) and n_{obs} is the number of observations at wavelengths $> 2.2 \mu\text{m}$.

Our second metric assumes that the IR excess is due to reprocessed stellar light (i.e. ignoring background IR emission and foreground circumstellar extinction). We approximate the amount of reprocessed light as being the integrated observed flux² longward

of $2.2 \mu\text{m}$ minus the integrated model flux over the same region. We can take this as a fraction of the underlying stellar flux, under the assumption that the total energy output (in Jy) of the star is not affected by circumstellar reprocessing of light. Mathematically, we can then define the fraction of stellar light reprocessed into the IR (L_{IR}/L_*) as

$$\frac{L_{\text{IR}}}{L_*} = \frac{\int_{2.2 \mu\text{m}}^{\infty} (F_{\nu}^{\text{obs}} - F_{\nu}^{\text{model}}) d\nu}{\int_0^{\infty} F_{\nu}^{\text{obs}} d\nu}. \quad (3)$$

We also define a wavelength, λ_{peak} , as where $\nu F_{\nu}^{\text{obs}} - \nu F_{\nu}^{\text{model}}$ reaches a peak. The precision with which we can define λ_{peak} depends strongly on the amount of available data.

3 MASTER CATALOGUE AND HR DIAGRAM

3.1 Presenting the catalogue

We are now in a position to list our data in a master catalogue containing the fundamental parameters of the *Hipparcos* stars. We do so in Table 2, which lists

- (i) column 1: the *Hipparcos* identifier for the object;
- (ii) columns 2 and 3: the coordinates of the object;
- (iii) columns 4 and 5: the parallax distance to the object and its associated fractional error;
- (iv) column 6: the modelled effective temperature of the object;
- (v) column 7: the modelled luminosity of the object;
- (vi) columns 8 and 9: the shortest and longest wavelength for which we have data;
- (vii) columns 10–30: the ratio of the observed to modelled flux at each wavelength, such that unity represents a perfect match to the model;
- (viii) column 31: n_{IR} , the number of observations at $\lambda > 2.2 \mu\text{m}$;
- (ix) column 32: E_{IR} , the average excess at those wavelengths, as defined above;
- (x) column 33: L_{IR}/L_* , the fraction of the object's luminosity reprocessed into the IR, as defined above;
- (xi) column 34: λ_{peak} , the wavelength at which the IR excess reaches a peak, as defined above.

The catalogue is displayed as an HR diagram in Fig. 1. The top panel of this figure shows the *Hipparcos* sample to separate out quite cleanly into the two traditional populations: the main-sequence stars, which are largely complete for stars brighter than a few solar luminosities, and the giant branch stars, which lie to cooler temperatures. The concentration of stars on the giant branch is due to two groups of stars. The first is the horizontal branch stars (which, since the sample is largely metal rich, form a red clump). The second is the RGB bump, the position which is also affected by metallicity (Cho & Lee 2002). A significant scatter of stars is seen away from these two groups, which is not necessarily real and which we discuss in Section 3.2.

3.2 Distance-limiting the sample and associated biases

Despite the removal of a significant amount of bad data, there is still a large amount of scatter in the HR diagram. There are four reasons for this. First, a large number of *Hipparcos* stars have relatively poor-quality data.³ These are mostly stars where there are insufficient IR

² Here, the flux is defined in energy terms, i.e. $\int F_{\nu} d\nu$ or $\int \lambda F_{\lambda} d\lambda$.

³ We refer here to noise over the entire SED, rather than one or two clearly mismatching ‘bad’ points.

Table 2. Fundamental parameters and IR excess for *Hipparcos* stars. The columns are described in the text. The complete table is available as Supporting Information with the online version of the paper.

HIP	RA (J2000)	Dec. (J2000)	d (pc)	$\delta d/d$	T_{eff} (K)	L (L_{\odot})	Coverage (nm)		SDSS u excess	...	IRAS [25] excess	n_{IR}	E_{IR}	$\frac{L_{\text{IR}}}{L_{\star}}$	λ_{peak} (μm)
							Start	End							
1	0.000 91	+01.089 01	219.78	0.29	6400	8.73	354	2200	0.872	...	0.000	0	0.000	0	0
2	0.003 80	−19.498 84	47.96	0.05	3300	3.11	354	623	1.077	...	0.000	0	0.000	0	0
3	0.005 01	+38.859 29	442.48	0.15	8968	374.87	420	8610	0.997	...	0.000	1	2.300	0.0019	8.6
...

data constraining the SED (these can be identified as those stars in Table 2 where n_{IR} , the number of measurements at $\lambda > 2.2 \mu\text{m}$, is small). This leads to a large fraction of the scatter observed in the HR diagram and to vertical artefacts (concentrations and rarefactions) on the BT-SETTL model grid spacing.

Secondly, stars which do have IR excess or suffer from substantial interstellar extinction scatter towards cooler temperatures (and, in the case of interstellar extinction, lower luminosities) in the HR diagram, as their optical light is either reprocessed into the IR or scattered out of the line of sight.

Thirdly, and perhaps most importantly, scatter arises from uncertainty in the *Hipparcos* parallax, which smears objects vertically in the HR diagram. This also leads to the Lutz–Kelker bias (Lutz & Kelker 1973). This bias occurs due to the inversion of parallactic angle to obtain a distance. As the measurement error is in parallax, this preferentially scatters objects to smaller distances. *Hipparcos* data suffer from this significantly. We use the benchmark of 17.5 per cent error in parallax (which corresponds to an average 30 per cent deviation in a set of stellar luminosities; Oudmaijer, Groenewegen & Schrijver 1998) as our figure of merit. Of the 107 619 stars in our final sample, only 49 188 have parallax errors less than this value. This rather severe limitation reduces the usefulness of the sample in examining stellar populations, particularly for the relatively rare stars on the upper giant branches. For many applications a wider sample, with increased Lutz–Kelker bias, is preferable. We therefore continue to include objects susceptible to significant Lutz–Kelker bias, but warn the reader to be mindful of its existence.

Finally, an additional distance error is present in red giants, where changes in brightness across the stellar surface (which covers a finite solid angle) cause a measurable astrometric shift. This can be misinterpreted as a parallactic shift, leading to much smaller *Hipparcos* distances than their true distance. This is perhaps best observed in the case of W Lyn, which has a *Hipparcos* parallax of $21.53 \pm 8.06 \text{ mas}$, despite being several kpc distant (Ita et al. 2001). This is an extreme case, though we warn the reader that no supposedly volume-limited sample of any consequence will be clean of all intruding objects for these reasons.

For the remainder of our analysis we adopt two volume-limited samples, which are subject to these biases at differing levels. The first is limited to stars with parallax distances of $<300 \text{ pc}$ with <30 per cent parallax errors, which have a wide range of data which cover the SED well ($\lambda_{\text{max}} > 2200 \mu\text{m}$). This subset of data still contains 46 869 of the original *Hipparcos* stars, of which 34 660 have parallax errors below 17.5 per cent. The second sample is distance limited to $<200 \text{ pc}$ with <30 per cent parallax errors, with the same requirement as that in which 32 741 out of 33 898 stars have errors <17.5 per cent in parallax. We refer to these in the discussion as the 300-pc and 200-pc samples, respectively.

4 DISCUSSION

4.1 Stellar isochrones

Much can be made of the HR diagram in terms of the star formation history of the local neighbourhood. However, to do so thoroughly requires a more in-depth analysis than we are able to provide in this work. As a cursory analysis, we present solar-metallicity Padova isochrones (Bertelli et al. 2008; Marigo et al. 2008) for a variety of ages in Fig. 2. The HR diagram is well described by a population of mixed age, but of near-solar metallicity.

Interstellar reddening does not appear to be a great cause of concern in the 200-pc sample in general, with the majority of stars lying within the bounds of the isochrones with only a few tenths of a magnitude of de-reddening at most. We show in Fig. 2 the effect that a reddening of $E(B - V) = 0.1 \text{ mag}$ has on particular sources chosen at a variety of different temperatures. We can see here that cooler sources are largely unaffected by this modest reddening, but that the effect becomes much more severe as the peak of the SED becomes bluer and the short-wavelength photometry available fails to constrain the SED. This may lead to underestimates of the temperatures and luminosities of some of the hotter stars. Particularly, errors can be large if short-wavelength data are unavailable or unusable.

4.2 Comparison to spectroscopic temperatures

With this in mind, we can check the consistency of our results, by comparing them to the spectroscopically derived temperatures of the NStars project (Gray et al. 2003, 2006). This project identifies the basic parameters of stars within 40 pc of the Sun by fitting moderately-high-resolution spectra; thus, the results are unbiased by interstellar reddening. Fig. 3 shows the ratio of their temperatures to ours for 407 stars we have in common. Examination of the three outliers (HIP 35550, 59199 and 71957) in this figure shows obvious problems with the 2MASS photometry that were missed by our bad data cuts. Neglecting these, the average temperature is consistent to <0.22 per cent (i.e. the error on the mean). The standard deviation of results is 4.4 per cent overall and decreases slightly towards lower temperatures.

Interstellar reddening should not affect the spectroscopic temperature, but imparts an apparent cooling to the photometric temperature, scattering points above unity. Four stars have a spectroscopic temperature >15 per cent higher than the photometric temperature: HIP 71193, 84379 (δ Her), 93805 (λ Aql) and 98495 (ϵ Pav). The latter two scatter in this direction due to excess flux in the *WISE* 4.6- μm band. The former two have SEDs that are poorly constrained by the input photometry. Unsurprisingly, we therefore find negligible reddening among stars within 40 pc.

In principle, with sufficiently-good-quality photometry, one could compute a three-dimensional extinction map of the Solar

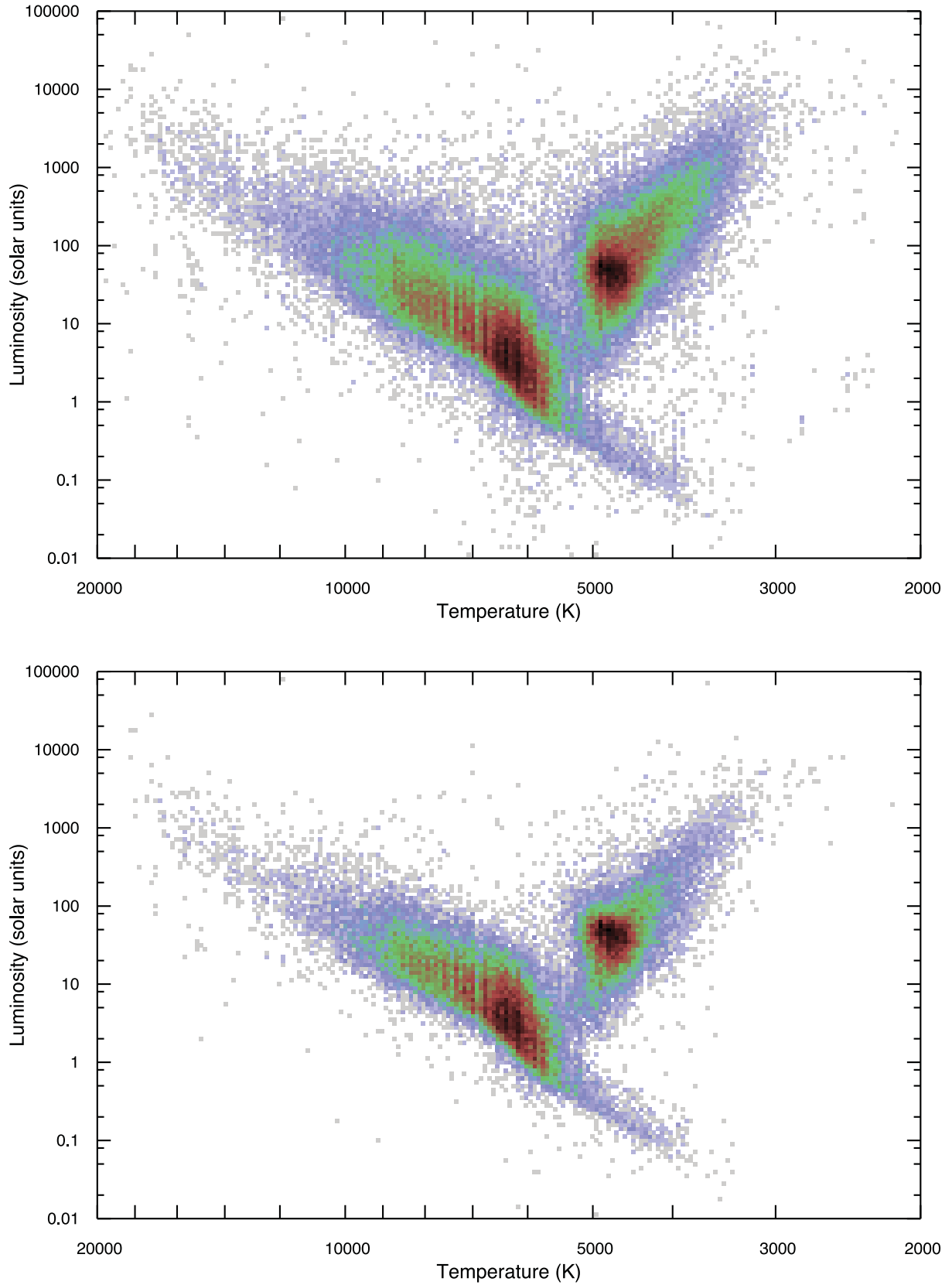


Figure 1. Density-coded HR diagram for the clipped *Hipparcos* data set, based on the BT-SETTL models. Top panel: stars with *Hipparcos* distances of < 1 kpc. Bottom panel: stars with *Hipparcos* distances of < 300 pc with parallax errors of < 30 per cent and photometric data at $> 2.2 \mu\text{m}$. Darker/redder colours show regions with a greater number of stars.

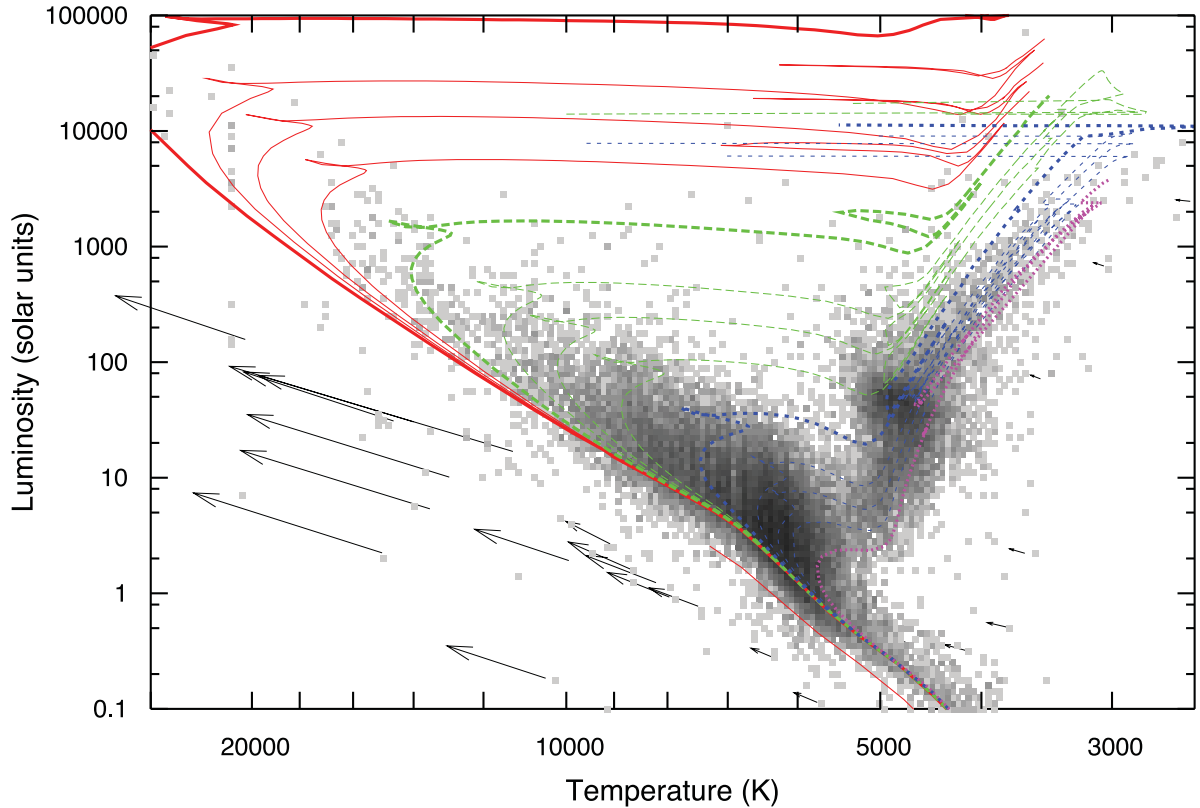


Figure 2. Density-coded HR diagram for the 200-pc sample (grey-scale). Overplotted are solar-metallicity isochrones from the Padova models (Bertelli et al. 2008; Marigo et al. 2008) at 10, 20, 30 and 50 Myr (solid, red lines); 100, 200, 300 and 500 Myr (long-dashed green lines); 1, 2, 3 and 5 Gyr (short-dashed blue lines) and 10 Gyr (dotted magenta line). The thin red line to the left of the main sequence is a zero-age isochrone at $[\text{Fe}/\text{H}] = -1$ to illustrate the blueward shift caused by decreasing metallicity. The black arrows show the effect of de-reddening individual sources by $E(B - V) = 0.1$ mag.

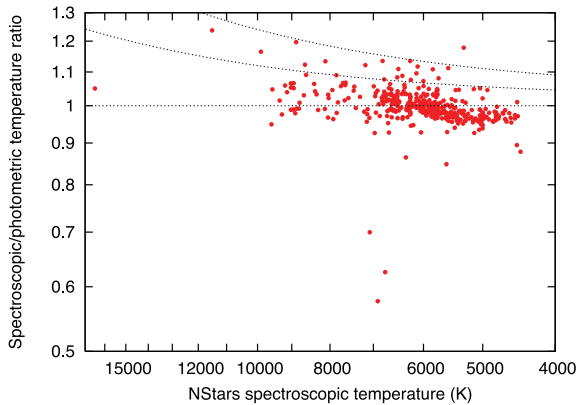


Figure 3. Comparison of our temperatures with those derived spectroscopically from the NStars project. The lines show the approximate deviations expected for $E(B - V) \approx 0.0, 0.1$ and 0.2 mag.

neighbourhood by comparing spectroscopically derived temperatures to photometrically derived temperatures. The lack of self-consistent photometry for the *Hipparcos* stars probably prevents such determination here, but may become possible in the *Gaia* era.

4.3 Grouping objects by type

The *AKARI-Hipparcos* catalogue of Ita et al. (2010) measures excess at 9 and 18 μm and contains grouping information for 2787 stars commonly exhibiting IR excess, including carbon stars, red giants, supergiants, S-type stars, etc. *AKARI* only detected 44 per

cent of the *Hipparcos* stars, so can be regarded as a selected subset of the *Hipparcos* sample, subject to its own biases. We remind the reader that the *Hipparcos* sample does not include all of the local (<300 pc) optically obscured giant stars, and that the compilation of stellar types listed in Ita et al. is only as complete as the literature from which they are based. The catalogue from Ita et al. (2010) cannot therefore be treated as a definitive, complete list of each type of sources, nor does it purport to be such. Of the 2787 classified stars in the list of Ita et al., we retain 2764 after removing bad data. Of these, only 749 meet the criteria for our 300-pc sample and 293 for our 200-pc sample.

The objects classified in Ita et al. (2010) within the 300-pc sample are presented on an HR diagram in Fig. 4. In general, the different types of stars match up well with their expected locations. M giants and S stars lie on the upper giant branch, along with the majority of carbon stars [we have not made an effort here to separate intrinsic from extrinsic carbon stars (Van Eck et al. 1998) due to the incomplete nature of any determination]. Be stars (which include a variety of hot, emission-line stars) are located in the upper-left of the HR diagram, but scatter towards temperatures cooler than the main sequence due to reprocessing of stellar light into the IR by the circumstellar excretion disc (cf. Kastner et al. 2006). Pre-main-sequence (pre-MS) stars likewise mostly lie towards the cooler side of the main sequence due to reprocessing of their optical emission into the IR, lowering the effective temperature.

The top panel of Fig. 5 shows a similar HR diagram, indicating the locations of the stars with greatest IR excess, as measured in terms of average fractional excess over the mid-IR spectrum (E_{IR}). The two regions of high stellar density (the main sequence above 6000 K,

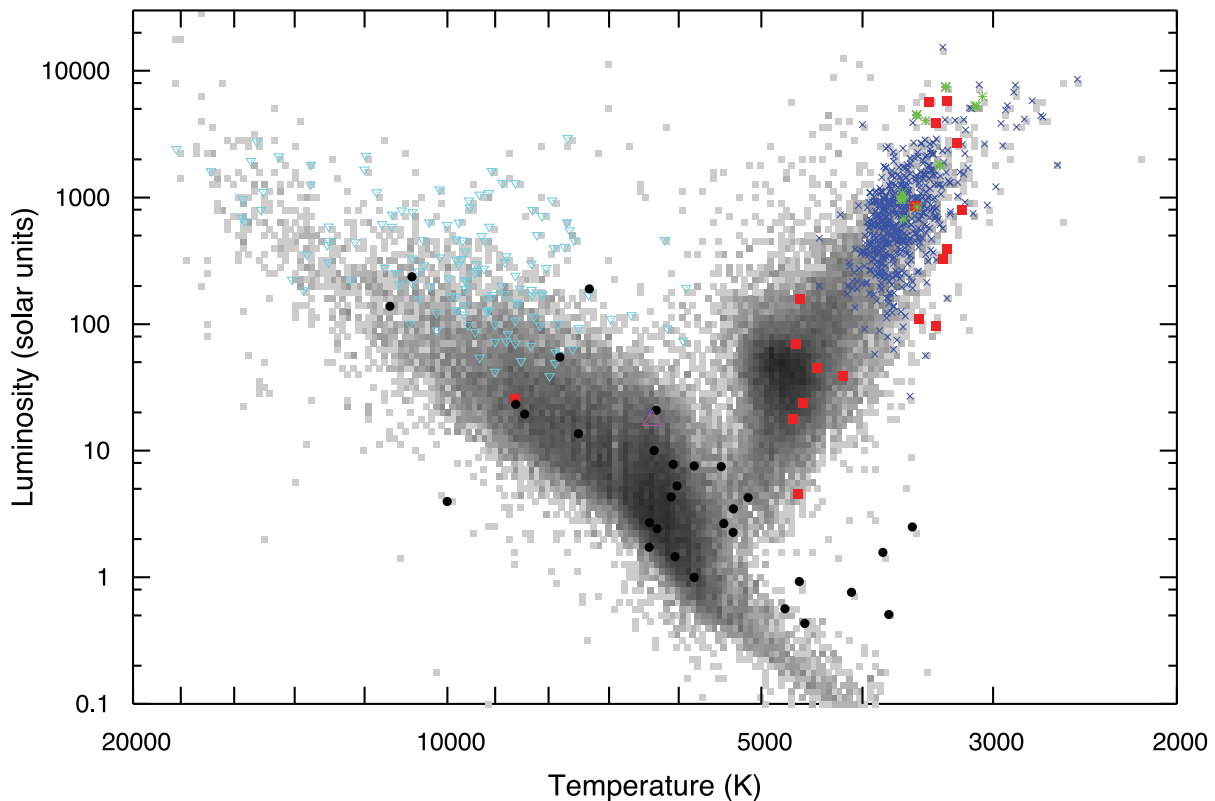


Figure 4. Density-coded HR diagram for the 300-pc sample (grey-scale, from the bottom panel of Fig. 1). The overplotted symbols are from Ita et al. (2010) and show known examples of the following. The black filled circles: pre-MS stars – cyan downward-pointing triangles: Be stars – large, magenta upward-pointing triangle: Wolf–Rayet star – blue crosses: M-type (super-)giants – green asterisks: S-type giants – red filled squares: carbon stars.

and the red clump) contain the largest number of IR-excessive stars. These stars are not usually truly excessive, except the case of several pre-MS stars, but are instead artificially reddened or suffer from source confusion in the IR. The majority of these stars are located near the Galactic plane or lie in or near the *IRAS* missing stripe and thus suffer from poor IR photometry. Some stars in the plane may suffer from sufficient interstellar extinction to appear to have IR excess, even at distances as small as 300 pc. Removing sources within 5° of the Galactic plane and the *IRAS* missing strip yields the HR diagram at the bottom of Fig. 5. The number of highly excessive sources is greatly reduced, with the few remaining sources of high excess located predominantly in the Gould Belt.

More pertinently, two further groups of IR-excessive stars in Fig. 5 are largely unchanged by this process. The first, above the main sequence at around 10 000 K, are identified as Be/Ae stars by Ita et al. (2010); the second are the cool, luminous stars near to and above the RGB tip. This second group are identified as M giants and S and carbon stars by Ita et al. (2010) and are likely to entirely be dust-producing AGB stars.

In Fig. 6, we show the different types of identified stars from Ita et al. (2010) as a function of our two measures of IR excess: E_{IR} and L_{IR}/L_* . While L_{IR}/L_* is a more physical measure of IR excess, E_{IR} is clearly more effective at separating out the IR-excessive stars from the bulk of the population, particularly for the Be stars.

Fig. 6 also shows a significant scatter below $E_{\text{IR}} = 1$. This represents a supposed deficit of IR flux in these stars and tends to be much more prevalent in the cooler stars. This is largely due to decreased sensitivity in stars further down the main sequence, but some upper giant branch stars also have IR deficits. In this case, scatter can be introduced by stellar variability, as photometry is not

usually averaged or taken contemporaneously, and does not imply either an instantaneous or time-averaged deficit in IR flux.

4.4 Giant stars with excess

Fig. 7 shows that scatter on the giant branch generally decreases as we approach the AGB tip, due to increased sensitivity on brighter sources. We can also see the substantial number of sources which have scattered to lower temperatures and higher values of E_{IR} (also Fig. 6), indicating reprocessing of optical light by circumstellar dust. The amount of excess around these stars can be correlated with their dust-production rate and hence their mass-loss rate. By identifying and characterizing individual stars which lie above the general scatter in Fig. 7, and including optically obscured sources missed by *Hipparcos*, we can make a theoretically complete census of dust-producing stars within 300 pc.

While that is beyond the scope of this paper, we do report on giant stars which are observed to have significant excess. We define this by $E_{\text{IR}} > 2.65 - \log(L)/3$ (see also Fig. 7), which is chosen to identify excesses of $\gtrsim 2\sigma$ at all luminosities. We list these stars in Tables 3 (luminous stars, above $850 L_\odot$) and 4 (stars below $850 L_\odot$). In these tables, we have also listed common names and spectral classification from SIMBAD, and variability information, sourced from either the General Catalogue of Variable Stars (GCVS; Samus et al. 2006; denoted ‘G’) or *Hipparcos* (denoted ‘H’) catalogues. Variability periods and amplitudes (either in the *Hipparcos* band, denoted as ‘H’; Johnson *V* band, denoted as ‘V’; or as a photographic measurement, denoted as ‘p’) are shown where available. Variability types are listed as follows: Mira = Mira variable; SRV = semi-regular variable;

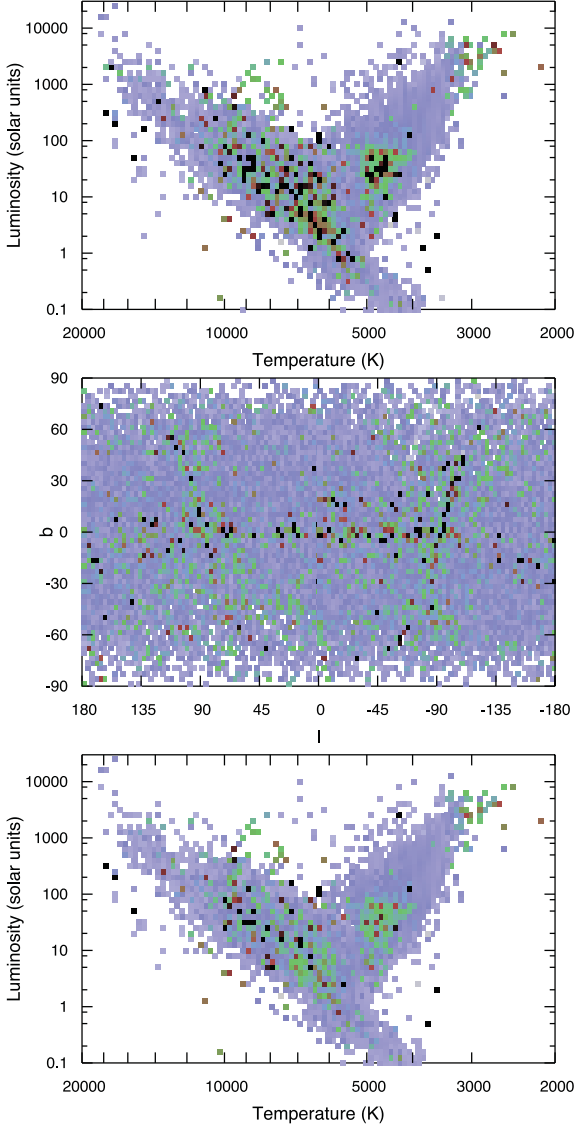


Figure 5. Top panel: HR diagram of the 300-pc *Hipparcos* sample. Bins are colour coded by IR excess (E_{IR}), with the colour coding denoting the object with the greatest excess in that bin: light blue indicates no excess ($E_{\text{IR}} = 1$), green indicates moderate excess ($E_{\text{IR}} \approx 2$), red strong excess ($E_{\text{IR}} \approx 5$) and black extreme excess (capped at $E_{\text{IR}} = 10$). Middle panel: as the top panel, but showing the Galactic distribution of those sources. Bottom panel: as the top panel, removing sources with $|b| < 5^\circ$ and within 5° of the IRAS missing strip.

Irr = irregular variable; V = unclassified variable; Bin = (eclipsing) binary; None = no appreciable variability. The spectral classifications of any *Infrared Astronomical Satellite* Low-Resolution Spectrometer (IRAS LRS) and *Infrared Space Observatory* Short Wavelength Spectrometer (ISO SWS) spectra of these sources are also given (Sloan & Price 1998; Sloan, Little-Marenin & Price 1998; Sloan et al. 2003; based on the classification method of Kraemer et al. 2002).

Table 3 contains some well-known targets, which are known to have substantial mass-loss. The spectral classification of the LRS and SWS spectra shows that most of these stars are known to have silicate features in their spectra and are therefore dust producers. Others, such as SS Lep, ϵ Car and α Her, are known to be binaries; therefore, their SEDs may not be well represented by a single black-

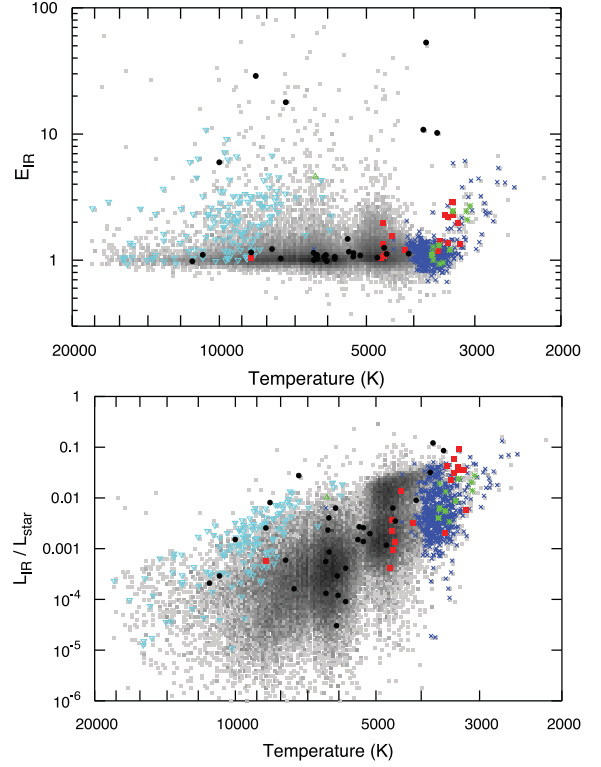


Figure 6. Measures of excess for different kinds of identified stars (see the text for definitions of E_{IR} and L_{IR}). The symbols are as in Fig. 4.

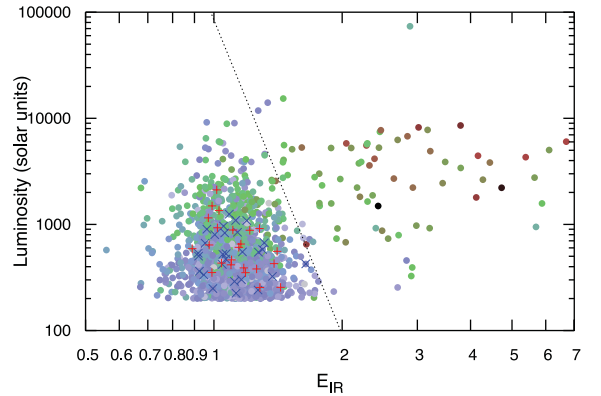


Figure 7. Excess among giant stars. Colour scale denotes the modelled stellar effective temperature: red points are coolest, and blue points are warmest. The red plus signs show stars from Groenewegen (2012) that were identified to have optical depths of $\tau_V > 10^{-5}$, and the blue crosses show those stars that were not. The dotted black line shows our definition of those stars with IR excess.

body (most giant stars, however, should outshine any companions at all wavelengths; note that α Her in particular is known to be dust producing; Tatebe et al. 2007). Several others without LRS or SWS spectra are likely to be mass-losing stars, but without IR spectra it is difficult to tell.

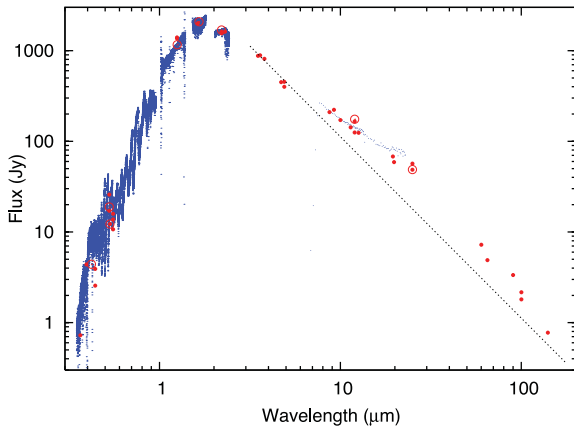
One outstanding example is present, however: that of EU Del (HIP 101810). Fig. 8 shows its SED. Literature photometry for this SED comes from the *Hipparcos*, *Tycho*, 2MASS, *AKARI* and *IRAS* catalogues already mentioned. Further photometry was sourced from Mermilliod's catalogue of homogeneous means (UBV; VizieR online data catalogue II/168), the Carlsberg Meridian Catalogue (V; Evans, Irwin & Helmer 1999), the catalogue of IR

Table 3. Literature spectroscopic and variability information for luminous ($>850 L_{\odot}$) giant stars with detected circumstellar emission. Details of columns and explanations of acronyms are listed in the text.

HIP	Name	Spectral type	Temperature (K)	Luminosity (L_{\odot})	Type	Amplitude (mag)	Band	Source	Period (d)	Source	LRS classification	SWS classification	E_{IR}
1728	T Cet	M5-6SIle	3329	7442	SRV	1.9	V	G	159	G	—	—	2.45
8565	TT Per	M5II-III	3228	1579	SRV	1.4	<i>p</i>	G	82	G	SE7	—	1.89
9234	V370 And	M7III	2948	3831	SRV	1.01	<i>H</i>	G	228	G	—	—	4.44
13064	Z Eri	M5III	3354	2334	SRV	1.63	V	G	80	G	SE8	—	1.79
17881	SS Cep	M5III	3158	5104	SRV	1.1	<i>p</i>	G	90	G	SE3	—	1.53
24169	RX Lep	M7	3256	3764	SRV	2.4	V	G	60	G	SE6	—	2.19
25194	SW Col	M1III	3661	921	V	0.34	V	G	—	—	SE8	—	2.40
27989	α Ori	M2Iab:	3659	73 524	SRV	1.3	V	G	2335	G	—	2.SEcp	2.88
28166	BQ Ori	M5IIIv	3192	917	SRV	2.1	V	G	110	G	—	—	1.95
28816	SS Lep	A1V+M6II	4347	2672	Bin	0.24	V	G	—	—	—	—	12.60
28874	S Lep	M5III	3187	3415	SRV	1.58	V	G	89	G	SE6t	—	3.79
36288	Y Lyn	M6SIb-II	3110	5249	SRV	2.5	V	G	110	G	—	—	2.10
38834	V341 Car	M0III	3326	1580	V	0.9	V	G	0	G	—	—	5.88
41037	ϵ Car	K3:IIIv+?	4209	14 086	Bin	0.08	<i>H</i>	G	0	G	—	—	1.34
42489	RV Hya	M5II	3200	1884	SRV	1.3	V	G	116	G	—	—	2.36
43215	AK Pyx	M5III	3410	1499	V	0.42	<i>H</i>	G	0	G	—	—	1.77
44050	RT Cnc	M5III	3192	2225	SRV	1.48	V	G	60	G	SE3	—	2.17
44862	CW Cnc	M6	2909	2228	V	1.2	<i>p</i>	G	—	—	SE3	—	2.93
45058	RS Cnc	M6IIIase	3122	5282	SRV	1.5	<i>p</i>	G	120	G	—	—	2.44
46806	R Car	M6.5IIIpev	2800	4164	Mira	6.6	V	G	309	G	SE1	—	2.38
48036	R Leo	M8IIIe	1995	1493	Mira	6.9	V	G	310	G	SE2	—	2.43
51821	U Ant	C5,3(Nb)	3317	5819	V	0.9	<i>p</i>	G	—	—	SiC+	—	2.29
52009	U Hya	C6.5,3(N2)	3400	3893	SRV	2.4	B	G	450	G	SiC	—	2.22
53809	R Crt	M7III	2491	8591	SRV	1.4	<i>p</i>	G	160	G	SE3t	—	3.79
57607	V919 Cen	M7III	3094	7766	SRV	0.58	<i>H</i>	G	—	—	—	—	3.17
61022	BK Vir	M7III:	2889	2706	SRV	1.52	V	G	150	G	SE4t	—	2.64
63642	RT Vir	M8III	2602	1804	SRV	1.29	V	G	155	G	SE3t	2.SEa	4.12
64569	SW Vir	M7III	2918	4917	SRV	1.5	V	G	150	G	SE3t	—	3.22
68357	RW CVn	M7III:	3141	973	SRV	1.1	<i>p</i>	G	100	G	SE2:	—	2.98
68815	θ Aps	M6.5III:	3151	3879	SRV	2.2	<i>p</i>	G	119	G	SE5t	2.SEb	3.48
69816	U UMi	M6e	3018	1821	Mira	5.9	V	G	331	G	SE2	—	2.20
70401	RX Boo	M7.5	2581	8196	SRV	2.67	V	G	162	G	SE3t	2.SEa	3.02
70969	Y Cen	M7III	2907	5317	Irr	1.1	<i>p</i>	G	180	G	SE1t	—	1.61
71802	RW Boo	M5III:	3148	3010	SRV	1.5	V	G	209	G	SE7	2.SEb	1.77
72208	EK Boo	M5III	3333	5587	SRV	0.38	<i>H</i>	G	—	—	—	—	1.46
76423	τ_4 Ser	M5II-III	3165	5264	SRV	1.18	V	G	100	G	SE4	—	1.88
77619	ST Her	M6-7IIIaS	3071	6270	SRV	1.5	V	G	148	G	SE1	2.SEa	2.70
78574	X Her	M8	3152	2765	SRV	1.1	V	G	95	G	SE6t	2.SEb	5.65
80488	U Her	M7III	2700	4438	Mira	7	V	G	406	G	SE4	2.SEc	4.16
80704	g Her	M6III	3261	4056	SRV	2	V	G	89	G	—	—	1.46
84345	α Her	M5Iab:	3351	15 368	Bin	1.26	V	G	—	—	—	1.NOOp	1.45
86527	BM Sco	K2.5Iab:	3676	949	SRV	1.9	<i>p</i>	G	815	G	—	—	5.69
94162	SZ Dra	M	3173	923	V	1	<i>p</i>	G	—	—	SE5	—	3.21
95413	CH Cyg	M7IIIv	2687	4316	Bin	2.89	V	G	—	—	—	2.SEc	5.39
95902	AF Cyg	M4	3305	1646	SRV	2	V	G	93	G	SE3t	—	2.29
98031	S Pav	M7IIe	2752	5563	SRV	3.8	V	G	381	G	SE2t	2.SEa	2.28
99082	V1943 Sgr	M7III	2752	5813	V	2	<i>p</i>	G	—	—	SE2t	2.SEa	2.04
99990	RT Cap	C6,4(N3)	3245	2683	SRV	2.8	<i>p</i>	G	393	G	SiC+	—	1.98
100935	T Mic	M7III	2856	7708	SRV	1.9	<i>p</i>	G	347	G	SE1t	2.SEa	2.46
101810	EU Del	M6III	3227	1585	SRV	1.11	V	G	60	G	N	—	1.77
104451	T Cep	M5-9	2866	6767	Mira	6.1	V	G	388	G	SE1	2.SEa	2.85
107516	EP Aqr	M8IIIv	3056	2651	SRV	0.45	V	G	55	G	SE5t	2.SEb	4.27
108928	TW Peg	M7.5IIIv	3145	5027	SRV	0.9	<i>p</i>	G	929	G	SE6t	—	6.11
110396	DZ Aqr	M	3055	2454	V	1.1	V	G	—	—	—	2.SEb	3.44
110428	BW Oct	M7III	2849	3592	V	0.9	<i>p</i>	G	—	—	SE5t	—	2.32
114318	Y Scl	M6III	3039	872	SRV	1.6	<i>p</i>	G	—	—	SE7	—	2.48
114404	V345 Peg	M3	3345	2795	V	0.37	<i>H</i>	G	—	—	—	—	1.72
117245	TX Psc	C7,2(N0)	3451	5693	V	0.41	V	G	—	—	N	1.NC	2.28
118188	R Cas	M7IIIe	2187	2219	Mira	8.8	V	G	431	G	SE5t	2.SEb	4.73

Table 4. Literature spectroscopic and variability information for less-luminous ($<1000 L_{\odot}$) giant stars with detected circumstellar emission. Details of columns and explanations of acronyms are listed in the text.

HIP	Name	Spectral type	Temperature (K)	Luminosity (L_{\odot})	Type	Amplitude (mag)	Band	Source	Period (d)	Source	LRS classification	SWS classification	E_{IR}
893	AC Cet	M3III	3413	793	SRV	0.33	V	G	—	—	—	—	2.71
39751	RU Pup	C5,4(N3)	3323	394	SRV	1.9	p	G	425	G	—	—	2.92
43438	RS Cam	M4III	3298	739	SRV	1.8	V	G	89	G	—	—	1.94
50916	HR 4091	K4III	4057	459	V	0.03	H	H	—	—	—	—	2.83
52656	TZ Car	C (R5)	3346	326	SRV	1.7	p	G	69	G	—	—	2.90
57800	RU Crt	M3	3054	681	V	1	p	G	—	G	SE3:	—	2.04
59389	HD 105822	K0/K1III	4464	234	None	0.03	H	H	—	—	—	—	1.91
59458	68 UMa	K5III	4478	256	None	0.04	H	H	—	—	—	—	2.70
71568	HR 5464	K4III	4214	727	None	0.05	H	H	—	—	—	—	1.68
112155	BD Peg	M8	3147	736	SRV	0.9	p	G	78	G	—	—	2.56

**Figure 8.** SED of EU Del. The large red points show literature photometry and the small blue points show literature spectra. The black line indicates the Rayleigh-Jeans tail expected for a dustless or ‘naked’ star. The references are listed in the text.

observations, including the Revised AGFL (Air Force Geophysics Laboratory) Infrared Sky Survey Catalog (4–20 μm ; Price & Murdock 1983; Gezari et al. 1993), Diffuse Infrared Background Experiment (DIRBE; 2.2–100 μm ; Price et al. 2010) and the *AKARI* Far-Infrared Surveyor (FIS) catalogue (65, 90 and 140 μm ; VizieR online data catalogue II/298). Literature spectroscopy for the optical (Valdes et al. 2004), *J* band (Wallace et al. 2000), *H* band (Meyer et al. 1998) and *K* band (Wallace & Hinkle 1997) is also shown, as is the *IRAS* LRS spectrum from Sloan & Price (1998). Sloan & Price (1998) classify EU Del as a naked star, as it shows no silicate feature. However, it is found to have substantial excess in both the *IRAS* [12] and [25] bands, and the IR spectrum clearly shows a rise above a blackbody towards longer wavelengths. Wu et al. (2011) place the star at a metallicity of $[\text{Fe}/\text{H}] = -1$, making it reminiscent of the featureless excesses we have previously found in metal-poor globular cluster giant stars (McDonald et al. 2010a, 2011a,d). We have previously attributed this to metallic iron dust on chemical and mineralogical grounds; however, it is spectrally indistinguishable from amorphous carbon dust and silicate dust composed primarily of large grains (cf. Höfner & Andersen 2007; Norris et al. 2012). EU Del may therefore be a unique nearby test-bed in which to determine which dust species is causing these unexplained featureless excesses.

Table 4 contains a few stars with suspected IR excess, which we examine more closely, in order to identify the luminosity at which

dust formation (as traced by IR excess) begins. We investigate these individually here.

(i) AC Cet: considerable excess exists in the *AKARI* [9] and [18] bands and the *IRAS* [12] and [25] bands. Chen et al. (2004) note that there is another evolved star within the *IRAS* PSF, but the excess in *AKARI* suggests that AC Cet does indeed have circumstellar dust. Kwok, Volk & Bidelman (1997) classify the source as having a class ‘C’ LRS spectrum, denoting an 11- μm SiC feature; however, this feature is tentative in this source, at best.

(ii) RU Pup: *AKARI*, *WISE* and *IRAS* data all show considerable excess at wavelengths longer than 4 μm . There is a significant scatter in the optical photometry, which leads to a poor estimation of the temperature and luminosity for this star. This may be partly due to its carbon richness and partly due to its variability. Bergeat & Chevallier (2005) place this star via two means at 2680 or 2875 K and 455 or 610 pc, which makes it considerably cooler and more luminous (1715 or 3649 L_{\odot}) than we model. This is corroborated by its long period (cf. Ita et al. 2004). It therefore probably suffers from the pulsation-induced distance errors we describe in Section 2.2.

(iii) RS Cam: this star also shows excess in the *AKARI*, *WISE* and *IRAS* data. Its short period suggests that its luminosity is correctly determined (cf. Ita et al. 2004). The LRS spectrum shows weak silicate emission (Kwok et al. 1997).

(iv) HR 4091: this source is modelled using *DIRBE* and *IRAS* data only. It shows marginal excess between 4 and 21 μm , and considerable excess in the *IRAS* [25] band. It is at very low Galactic latitude ($b = -0.5$) and thus suffers from considerable contamination from surrounding sources. We therefore do not believe this excess is real.

(v) TZ Car: the 8- to 25- μm data for this star show considerable excess. Reprocessing of the *Hipparcos* data by Knapp, Pourbaix & Jorissen (2001) suggests that the distance for this star is roughly correct. At a Galactic latitude of $b = -5.8$, TZ Car may suffer from some extinction, but it is likely that the excess and parameters are sufficiently correct to say that this star is losing mass.

(vi) RU Crt: a known mass-losing star; this star shows moderate excess in the *AKARI* bands and substantially more excess in the *IRAS* bands. At 132 pc, it is possible that more extended emission is missed by *AKARI*: sources up to roughly this distance may have some emission outwith the *AKARI* beam at 25 μm (see Section 4.5).

(vii) HD 105822: this star is in a region of high projected stellar density ($b = -5.7$). The amount of excess for this star is inconsistent across the IR data, varying among the surveys and bands. A dubious *J*-band flux probably suggests more IR excess than is

truly present. The apparent IR excess in this case is likely due to source blending and confusion, coupled with poor-quality short-wavelength photometry.

(viii) 68 UMa: this star is mistakenly classified as excessive due to a mismatch between the *Hipparcos*/*Tycho* magnitudes and those from the SDSS, which differ by approximately a magnitude, despite no variability being detected by *Hipparcos*. This has led to an excess being determined incorrectly. By using a variety of combinations of photometry, we estimate that a correct temperature and luminosity of around 4000 K and 400 L_{\odot} would be more appropriate for this source, and that it has no substantial reddening.

(ix) HR 5464: the determination of IR excess for this star is based solely on the *IRAS* data, in which excess is relatively weak (86 per cent at 12 μm , 50 per cent at 25 μm). *DIRBE* data suggest that there is little or no IR excess for this source.

(x) BD Peg: a known mass-losing star; Kwok et al. (1997) note that silicate emission is present in this object and Gezari et al. (1993) confirm its IR excess.

With the exception of the carbon star TZ Car, we therefore find no detectable dust production by any object below the luminosity of RU Crt (681 L_{\odot}). We therefore conclude that this represents the luminosity at which dust production by AGB stars begins in earnest in the local neighbourhood. This corroborates very well with the $\approx 700 L_{\odot}$ we have previously found in Galactic globular clusters (Boyer et al. 2009a; McDonald et al. 2009, 2011b,d).

4.5 Comparison to Groenewegen (2012)

We now turn our attention to the work of Groenewegen (2012). This paper identifies several low-luminosity *Hipparcos* stars with IR excess which Groenewegen attributes to weak dust emission. These stars have much lower luminosities (50–350 L_{\odot}) than those we find excess around, as Groenewegen was examining RGB stars for dust excesses much smaller than we have deemed accurately determinable in this work.

The stars from Groenewegen (2012) which have survived our data quality cuts are shown in Fig. 7. Groenewegen purposely targeted stars with low ($V - I$) colours; thus, his sample does not include stars from with high values of E_{IR} . It is notable, however, that all 52 stars common to our data sets lie within the scatter of points with no unusual IR excess. Also, Groenewegen's dusty stars appear to have no more IR excess than his dustless stars.

The reasons behind this are not immediately obvious, but can be understood by examining the subtle differences between our analyses. The most striking of these is the choice of input data. We have included data from *WISE*, *AKARI* [9] and [18] and *IRAS* [12] and [25]. Groenewegen includes data from *AKARI* (including the far-IR 60- and 90- μm FIS bands) and *IRAS* (including the far-IR 60- and 100- μm bands).

The choice of whether or not to include the far-IR data is a balance of gaining sensitivity to cold dust and acquiring systematic errors due to contamination in the line of sight. The issue with the *AKARI* FIS and *IRAS* data we have excluded is the beam size (37 and 39 arcsec for *AKARI* FIS 60 and 100 μm , respectively;⁴ 4.5 arcmin \times 0.7 arcmin for *IRAS* 12 μm ; Miville-Deschênes & Lagache 2005). These are much larger than the beam sizes for the other IR data (5.6 arcsec for *AKARI* IRC 8.6 μm ;⁵

7.36 arcsec \times 6.08 arcsec for *WISE* 11.6 μm ⁶) and much larger than the optical photometry (typically 1–2 arcsec). A large PSF full width half-maximum (PSF FWHM) means there is a substantial issue with contamination from unrelated sources in the line of sight, from diffuse background emission or from interstellar medium headed by the star. Equally, if a giant star has a spatially extended wind, this may be missed by only considering data with a small PSF. Groenewegen has been careful to exclude sources with strong cirrus contamination, which is the main contaminant in the *IRAS* photometry. However, his exclusions are based on the 100- μm images, whereas ecliptic dust is a greater contaminant at 25 and 60 μm . These sources would therefore not be identified as contaminated.

On examining the individual stars which Groenewegen (2012) claims are dusty, we find that the comparatively large PSF size of *IRAS* and (in some cases) *AKARI* FIS appears to be the primary cause of the difference between our data sets. Typically, the *IRAS* [12] and [25] flux is systematically in excess of the modelled stellar photosphere compared to the smaller PSF *AKARI* IRC and *WISE* photometry. As an example, we model HIP 44126 (FZ Cnc) to have moderate excess in *IRAS* (52 and 35 per cent at 12 and 25 μm), but little excess in *WISE* (8 and 6 per cent at 11.6 and 22.1 μm). By only taking the *IRAS* data, Groenewegen naturally models this star as having reasonable IR excess. In this particular instance, the contaminating source can be clearly identified as poorly subtracted emission from warm dust in the ecliptic plane in the original *IRAS* photometry. The same is true of HIP 53449, though here are the *AKARI* FIS data that suffer from contamination from the ecliptic.

Not all of Groenewegen's dusty sources can be explained so easily, however. Both HIP 67605 and 67665 (AW CVn) are identified as dusty by Groenewegen (2012). They lie quite close to each other (15 arcmin apart) but are resolved in the *IRAS* images by several beam widths. They do not suffer from substantial contamination. They are covered by *AKARI* and *IRAS*, but not the *WISE* preliminary catalogue. Both sources have excess at *IRAS* [12] and [25] but not *AKARI* [9] and [18]. Like the majority of Groenewegen's targets, these stars lie at around 200 pc. At this distance the *AKARI* 8.6- μm PSF has an FWHM of 1120 au or 2000–4000 stellar radii. Assuming that the dust temperature approximately follows a $T^4 \propto R^2$ law, and a stellar temperature of ≈ 3700 K, this implies that dust falling within the *IRAS* beam but outwith the *AKARI* IRC beam should emit with a peak wavelength of $\lambda \gg 35 \mu\text{m}$. It should therefore not emit significantly at 8–18 μm to cause the discrepancy between the *AKARI* near-IR and *IRAS* [12] fluxes.

Nevertheless, the IR excess Groenewegen finds may still be real, and still be related to a wind emanating from the star. Two situations may cause this. The first case is that a cooler, detached shell surrounds the star and emits only at longer (60–100 μm) wavelengths (cf. Y CVn; Libert, Gérard & Le Bertre 2007). In the second case, the emission would not be produced by the star, but instead by the interstellar dust swept up in a bow shock around the astropause (Wareing et al. 2007). This has been seen in other nearby AGB stars (Ueta et al. 2006, 2010; Ladjal et al. 2010) and could be the source of the excess emission at longer (60–100 μm) wavelengths that Groenewegen finds in several cases.

We also acknowledge that variability may also play a role in this analysis. Neither Groenewegen's nor our determinations of IR excess take into account the variability of stars. As Groenewegen

⁵ From the *AKARI* NIR data user manual, version 1.3: http://www.sciops.esa.int/SA/ASTROF/docs/IRC_IDUM_1.3.pdf

⁴ From the *AKARI* FIS data user manual, version 1.3: http://www.ir.isas.jaxa.jp/ASTRO-F/Observation/IDUM/FIS_IDUM_1.3.pdf

⁶ From the *WISE* preliminary release explanatory supplement: http://wise2.ipac.caltech.edu/docs/release/prelim/expSUP/sec4_5c.html

(2012) uses some different optical data to ours, we may find that some stars in both studies appear to have IR excess simply because their optical photometry was observed when the star was at photometric minimum. Conversely, excess might be missed if observations were carried out at photometric maximum.

Groenewegen (2012) and this work probe subtly different data sets with subtly different techniques. It should therefore not be surprising that we find different results, though we would argue that our analysis should be better suited to finding ongoing dust production by stars. On the basis of the above discussion, we advise caution when investigating small IR excesses in such cases and note the benefits of phase-matched, high-resolution IR photometry (see also Sloan et al. 2010; McDonald et al. 2011b; Momany et al. 2012).

5 CONCLUSIONS

In this work, we have demonstrated the use of SED fitting to determine the fundamental parameters of the *Hipparcos* star sample. We have further used this information to quantify excess flux over the entire optical, and near- and mid-IR region of each SED. We have combined these excesses to determine those stars showing an excess of IR flux, and cross-correlated literature identifications to examine the cause of that excess over different regions of the HR diagram, comparing our results to the key studies of Ita et al. (2010) and Groenewegen (2012). We find we cannot reproduce the IR excess and dust production claimed by the latter paper.

Our analysis has focused on the *Hipparcos* data catalogue: data which are now over 20 yr old and, despite showing their age, provide the best estimate of distances to nearby stars we have. The launch of *Gaia* and the completion of further all-sky surveys, such as Panoramic Survey Telescope and Rapid Response System (Pan-STARRS), SDSS and *WISE*, will allow a similar analysis to be performed on many times more objects. Automated techniques, building on the kind demonstrated here, will be necessary to analyse and classify the objects which come from these surveys, in order to gain a full and comprehensive understanding of our corner of the Galaxy and its inhabitants.

ACKNOWLEDGMENTS

We thank Martin Groenewegen for his invaluable input into the comparison with his published works and his help in resolving the differences between our results.

This research has made extensive use of the SIMBAD data base, VizieR catalogue access tool and Aladin, operated at CDS, Strasbourg, France.

This research has made use of the NASA/IPAC Infrared Science Archive, which is operated by the Jet Propulsion Laboratory, California Institute of Technology, under contract with the National Aeronautics and Space Administration.

The *Hipparcos*/*Tycho* catalogues are a result of the *Hipparcos* space astrometry mission, undertaken by the European Space Agency.

Funding for SDSS-III has been provided by the Alfred P. Sloan Foundation, the Participating Institutions, the National Science Foundation and the U.S. Department of Energy. The SDSS-III website is <http://www.sdss3.org/>.

The DENIS project has been partly funded by the SCIENCE and the HCM plans of the European Commission under grants CT920791 and CT940627. It is supported by INSU, MEN and CNRS in France, by the State of Baden-Württemberg in Germany,

by DGICYT in Spain, by CNR in Italy, by FFwFBWF in Austria, by FAPESP in Brazil, by OTKA grants F-4239 and F-013990 in Hungary and by the ESO C&EE grant A-04-046. Jean Claude Renault from IAP was the Project manager. Observations were carried out thanks to the contribution of numerous students and young scientists from all involved institutes, under the supervision of P. Fouqué, survey astronomer resident in Chile.

This publication makes use of data products from the Two Micron All Sky Survey, which is a joint project of the University of Massachusetts and the Infrared Processing and Analysis Center/California Institute of Technology, funded by the National Aeronautics and Space Administration and the National Science Foundation.

This research made use of data products from the Midcourse Space Experiment. Processing of the data was funded by the Ballistic Missile Defense Organization with additional support from NASA Office of Space Science.

This publication makes use of data products from the *Wide-field Infrared Survey Explorer*, which is a joint project of the University of California, Los Angeles, and the Jet Propulsion Laboratory/California Institute of Technology, funded by the National Aeronautics and Space Administration.

This research is based on observations with *AKARI*, a JAXA project with the participation of ESA.

REFERENCES

- Aihara H. et al., 2011, *ApJS*, 193, 29
- Allard F., Guillot T., Ludwig H.-G., Hauschildt P. H., Schweitzer A., Alexander D. R., Ferguson J. W., 2003, in Martín E., ed., *Proc. IAU Symp.* 211, Brown Dwarfs. Astron. Soc. Pac., San Francisco, p. 325
- Beichmann C. A., Helou G., Walker D. W., 1988, *Infrared Astronomical Satellite (IRAS). Catalogs and Atlases*. NASA, Washington
- Bergeat J., Chevallier L., 2005, *A&A*, 429, 235
- Bertelli G., Girardi L., Marigo P., Nasi E., 2008, *A&A*, 484, 815
- Boyer M. L. et al., 2009a, *ApJ*, 705, 746
- Boyer M. L., Skillman E. D., van Loon J. T., Gehrz R. D., Woodward C. E., 2009b, *ApJ*, 697, 1993
- Chen P. S., Gao Y. F., Shan H. G., Wang X. H., 2004, *New Astron.*, 9, 17
- Cho D.-H., Lee S.-G., 2002, *AJ*, 124, 977
- Dotter A., Chaboyer B., Jevremović D., Kostov V., Baron E., Ferguson J. W., 2008, *ApJS*, 178, 89
- Egan M. P., Price S. D., 1996, *AJ*, 112, 2862
- Evans D. W., Irwin M. J., Helmer L., 2002, *A&A*, 395, 347
- Gezari D. Y., Schmitz M., Pitts P. S., Mead J. M., 1993, *Catalog of Infrared Observations*, 3rd edn (RP-1294). NASA, Washington.
- Gray R. O., Corbally C. J., Garrison R. F., McFadden M. T., Robinson P. E., 2003, *AJ*, 126, 2048
- Gray R. O., Corbally C. J., Garrison R. F., McFadden M. T., Bubar E. J., McGahee C. E., O'Donoghue A. A., Knox E. R., 2006, *AJ*, 132, 161
- Groenewegen M. A. T., 2012, *A&A*, 540, A32
- Gustafsson B., Bell R. A., Eriksson K., Nordlund A., 1975, *A&A*, 42, 407
- Gustafsson B., Edvardsson B., Eriksson K., Jørgensen U. G., Nordlund Å., Plez B., 2008, *A&A*, 486, 951
- Höfner S., Andersen A. C., 2007, *A&A*, 465, L39
- Ita Y., Deguchi S., Fujii T., Kameya O., Miyoshi M., Nakada Y., Nakashima J., Parthasarathy M., 2001, *A&A*, 376, 112
- Ita Y. et al., 2004, *MNRAS*, 347, 720
- Ita Y. et al., 2010, *A&A*, 514, A2
- Kastner J. H., Buchanan C. L., Sargent B., Forrest W. J., 2006, *ApJ*, 638, L29
- Knapp G., Pourbaix D., Jorissen A., 2001, *A&A*, 371, 222
- Kraemer K. E., Sloan G. C., Price S. D., Walker H. J., 2002, *ApJS*, 140, 389
- Kwan J., Hill F., 1977, *ApJ*, 215, 781
- Kwok S., Volk K., Bidelman W. P., 1997, *ApJS*, 112, 557

- Ladjal D. et al., 2010, *A&A*, 518, L141
 Libert Y., Gérard E., Le Bertre T., 2007, *MNRAS*, 380, 1161
 Luck R. E., Heiter U., 2005, *AJ*, 129, 1063
 Lutz T. E., Kelker D. H., 1973, *PASP*, 85, 573
 Marigo P., Girardi L., Bressan A., Groenewegen M. A. T., Silva L., Granato G. L., 2008, *A&A*, 482, 883
 McDonald I., van Loon J. T., Decin L., Boyer M. L., Dupree A. K., Evans A., Gehr R. D., Woodward C. E., 2009, *MNRAS*, 394, 831
 McDonald I., Sloan G. C., Zijlstra A. A., Matsunaga N., Matsuura M., Kraemer K. E., Bernard-Salas J., Markwick A. J., 2010a, *ApJ*, 717, L92
 McDonald I., van Loon J. T., Dupree A. K., Boyer M. L., 2010b, *MNRAS*, 405, 1711
 McDonald I., Boyer M. L., van Loon J. T., Zijlstra A. A., 2011a, *ApJ*, 730, 71
 McDonald I. et al., 2011b, *ApJS*, 193, 23
 McDonald I., Johnson C. I., Zijlstra A. A., 2011c, *MNRAS*, 416, L6
 McDonald I. et al., 2011d, *MNRAS*, 417, 20
 Meyer M. R., Edwards S., Hinkle K. H., Strom S. E., 1998, *ApJ*, 508, 397
 Miville-Deschênes M.-A., Lagache G., 2005, *ApJS*, 157, 302
 Momany Y., Saviane I., Smette A., Bayo A., Girardi L., Marconi G., Milone A. P., Bressan A., 2012, *A&A*, 537, A2
 Moshir M. et al., 1992, Explanatory Supplement to the IRAS Faint Source Survey, Version 2: JPL D-10015 8/92. Jet Propulsion Laboratory, Pasadena, CA
 Norris B. R. M. et al., 2012, *Nat*, 484, 220
 Oudmaijer R. D., Groenewegen M. A. T., Schrijver H., 1998, *MNRAS*, 294, L41
 Perryman M. A. C. et al., 1995, *A&A*, 304, 69
 Perryman M. A. C., ESA, eds., 1997, ESA SP, Vol. 1200, The Hipparcos and Tycho Catalogues. Astrometric and Photometric Star Catalogues Derived From The ESA Hipparcos Space Astrometry Mission. ESA, Noordwijk
 Price S. D., Murdock T. L., 1983, The Revised AFGL Infrared Sky Survey Catalog (AFGL-IR-83-0161). Air Force Geophysics Laboratory, Hanscom
 Price S. D., Smith B. J., Kuchar T. A., Mizuno D. R., Kraemer K. E., 2010, *ApJS*, 190, 203
 Samus N. N., Durlevich O. V., Zharova A. V., Kazarovets E. V., Kireeva N. N., Pastukhova E. N., Williams D. B., Hazen M. L., 2006, *Astron. Lett.*, 32, 263
 Skrutskie M. F. et al., 2006, *AJ*, 131, 1163
 Sloan G. C., Price S. D., 1998, *ApJS*, 119, 141
 Sloan G. C., Little-Marenin I. R., Price S. D., 1998, *AJ*, 115, 809
 Sloan G. C., Kraemer K. E., Price S. D., Shipman R. F., 2003, *ApJS*, 147, 379
 Sloan G. C. et al., 2010, *ApJ*, 719, 1274
 Tatebe K., Hale D. D. S., Wishnow E. H., Townes C. H., 2007, *ApJ*, 658, L103
 Ueta T. et al., 2006, *ApJ*, 648, L39
 Ueta T. et al., 2010, *A&A*, 514, A16
 Valdes F., Gupta R., Rose J. A., Singh H. P., Bell D. J., 2004, *ApJS*, 152, 251
 Van Eck S., Jorissen A., Udry S., Mayor M., Pernier B., 1998, *A&A*, 329, 971
 van Leeuwen F., 2007, *A&A*, 474, 653
 Wallace L., Hinkle K., 1997, *ApJS*, 111, 445
 Wallace L., Meyer M. R., Hinkle K., Edwards S., 2000, *ApJ*, 535, 325
 Wareing C. J., Zijlstra A. A., O'Brien T. J., Seibert M., 2007, *ApJ*, 670, L125
 Woods P. M. et al., 2011, *MNRAS*, 411, 1597
 Wright E. L. et al., 2010, *AJ*, 140, 1868
 Wu Y., Singh H. P., Prugniel P., Gupta R., Koleva M., 2011, *A&A*, 525, A71

APPENDIX A: REMOVAL OF BAD DATA

We describe in this appendix the sequentially applied cuts we use to remove bad data from our catalogue.

A1 Cut #1

The first cut was designed to remove extremely cool sources and sources with distinctly double-peaked SEDs from the sample. These tend to be heavily enshrouded or heavily extincted objects which we cannot accurately model.

Stars were removed from the main catalogue if they had at least two mid-IR (3.5–25 μ m) bands brighter than all their optical/near-IR ($u'-K_s$ band) data. This cut removed 241 objects from the catalogue, of which 98 objects have no *IHK_s*-band data, leaving 109 436.

A2 Cut #2

The second cut was designed to remove unphysically low values from the *WISE* data, which are much too faint to come from a stellar object detectable by *Hipparcos*. A *WISE* photometric datum was removed from the combined catalogue if its flux was below 100 μ Jy. In this way, *WISE* photometry was deleted from 281 objects.

A3 Cut #3

The third cut acts to remove more underluminous W_1 and W_2 data. To assist in this, we define two fluxes, F_{10} and F_{20} : F_{10} is the 10- μ m flux defined by (in order of preference) the W_3 , *AKARI* [9] or *IRAS* [12] flux, and F_{20} is defined similarly by the W_4 , *AKARI* [18] or *IRAS* [25] flux.

This cut applies to all stars where $F_{10} > F_{20}$ and stars where no F_{10} measurement exists. This requirement prevents the selection of dusty sources where the SED reaches a minimum between 3 and 8 μ m, but where dust emission is insufficient to be picked up by Cut #1. W_1 and/or W_2 are removed if their fluxes are less than 40 per cent of both the 2MASS (or DENIS, where substituted) K_s -band and the F_{10} fluxes. Where no measure of F_{10} is available, F_{20} is used instead.

The cut removes *WISE* data from 273 objects.

A4 Cut #4

The fourth cut removes more underluminous W_1 data. This cut detects objects where the flux in W_1 is <40 per cent of the flux in W_2 , provided the flux in W_2 is: (1) non-zero, (2) greater than the flux in W_3 and (3) less than the flux in K_s (where W_3 and K_s fluxes exist). The Cepheid X Sgr (HIP 87072) is excluded from this cut as a special case. This removes 38 bad W_1 data points from the catalogue.

At this point, sources were also removed from the catalogue if they had data in five or fewer of the observed bands. This removed 1479 objects, leaving 107 957. Most of the deletions were either detected by *Hipparcos* and *IRAS*, or *Hipparcos* and SDSS.

A5 Cut #5

The fifth cut is designed to remove single bad photometric data points. It operates on all filters shortward of 8.6 μ m, except the *Hipparcos*/*Tycho* data.

For each *Hipparcos* object, we determine the worst-fitting filter out of those listed in the previous paragraph, i.e. the filter with the greatest value of R or $1/R$. If this value is five times greater than the next largest R or $1/R$, it is removed. For example, if J and K_s are the two worst-fitting filters, $R_J = 51$ and $R_{K_s} = 10$, then the J -band datum will be removed, whereas if $R_J = 49$ it will not.

This cut removes 78 bad data points from the catalogue. Of these, 60 are DENIS *I*-band fluxes.

A6 Cut #6

The sixth cut was done manually to remove five stars where IR photometry is clearly confused due to blending, variability or background. These stars are HIP 60782, 80057 and 88267 (all binaries), and HIP 82850 and 82611. This left 107 952 unique catalogued objects.

A7 Cut #7

The seventh cut removes *MSX* B_1 and/or B_2 data when these data have a higher flux than the K_s filters and one of the W_3 , *AKARI* [9] or *IRAS* [12] filters. While in principle this could remove points from SEDs peaking between 2.2 and 12 μm , no objects seem to be affected by this. Dustless stars tend to peak at wavelengths shorter than 2.2 μm , while dusty stars with double-peaked SEDs tend to have their second peak at wavelengths longer than 12 μm . Data were removed from 244 objects, though this affected only fraction of these, as *MSX* data are only used when *WISE* data are unavailable. There were 13 objects removed during this stage because they had insufficient photometry, leaving 107 939 unique objects.

A8 Cut #8

The eighth cut is designed to remove underluminous SDSS data from saturated sources. SDSS *g*- and/or *r*-band data are removed if they are recorded to have less flux than the *Hipparcos* and *Tycho*

B_T and V_T fluxes. This affects 7058 objects, though most of these were already rejected in Section 2.1.

An additional 224 points were manually removed from 147 objects, mainly consisting of errant W_1 and W_2 fluxes. A further 39 objects were rejected for having insufficient data, leaving 107 900 unique objects.

A9 Cut #9

The ninth cut repeats cut #5, removing data points which have a goodness of fit more than a factor of 2.5 (instead of 5) worse than the next worst-fitting point. This cut was performed in two iterations: the first removing a point from 647 objects and the second removing a point from 59 objects. A final 120 points from 112 objects were edited out by hand. Following this, objects with less than five photometric points at $<8 \mu\text{m}$ were rejected, leaving 107 619 unique objects in the final catalogue.

SUPPORTING INFORMATION

Additional Supporting Information may be found in the online version of this paper:

Table 2. Fundamental parameters and IR excess for *Hipparcos* stars. Please note: Wiley-Blackwell are not responsible for the content or functionality of any supporting materials supplied by the authors. Any queries (other than missing material) should be directed to the corresponding author for the paper.

This paper has been typeset from a $\text{\TeX}/\text{\LaTeX}$ file prepared by the author.